Title: Thermodynamic modelling of Sol Hamed serpentinite, South Eastern Desert of Egypt: implication for fluid interaction in the Arabian-Nubian Shield ophiolites

Article Type: Research Paper

Abstract: The Arabian-Nubian Shield is the largest tract of juvenile continental crust of the Neoproterozoic. This crust was generated due to arc-arc collision associated with the closing of the Mozambique Ocean, and ophiolitic rocks mark suture zones in the shield. The Sol Hamed ophiolite in the southeastern Egypt defines a near-source tectonic facies, representing an uncommon example of rocks that might be less deformed due to the movement far from the corresponding suture. In order to understand fluid-rock interactions before and during arc-arc collision, petrological, mineral chemistry, whole-rock chemistry and thermodynamic studies were applied to the Sol Hamed serpentinized ophiolitic mantle fragment. These studies reveal that the protolith had a harzburgite composition that probably originated as forearc mantle. Protolith alteration resulted from two stages of fluid-rock interaction. The first stage occurred as a result of infiltration of concentrated CO_2-rich fluid released from carbonate bearing sediments and altered basalt at the subduction zone. The alteration occurred during isobaric cooling at a pressure of 1 kbar. The fluid composition during the isobaric cooling was buffered by the metamorphic reactions. The second stage of fluid-rock interactions took place through prograde metamorphism. The increase in pressure during this stage occurred as a result of thrusting within the oceanic crust. In this process the forearc crust was loaded by roughly 20-30 km of overthrust rocks.

Abstract

The Arabian-Nubian Shield is the largest tract of juvenile continental crust of the Neoproterozoic. This crust was generated due to arc-arc collision associated with the closing of the Mozambique Ocean, and ophiolitic rocks mark suture zones in the shield. The Sol Hamed ophiolite in ~~the~~ southeastern Egypt defines a near-source tectonic facies, representing an uncommon example of rocks that might be less deformed due to the movement far from the corresponding suture. In order to understand fluid-rock interactions before and during arc-arc collision, petrological, mineral chemistry, whole-rock chemistry and thermodynamic studies were applied to the Sol Hamed serpentinized ophiolitic mantle fragment. These studies reveal that the protolith had a harzburgite composition that probably originated as forearc mantle. Protolith alteration resulted from two stages of fluid-rock interaction. The first stage occurred as a result of infiltration of concentrated CO_2-rich fluid released from carbonate bearing sediments and altered basalt at the subduction zone. The alteration occurred during isobaric cooling at a pressure of 1 kbar. The fluid composition during the isobaric cooling was buffered by the metamorphic reactions. The second stage of fluid-rock interactions took place through prograde metamorphism. The increase in pressure during this stage occurred as a result of thrusting within the oceanic crust. In this process the forearc crust was loaded by roughly 20-30 km of overthrust rocks.

- Sol Hamed ophiolitic has a harzburgite composition as protolith

- The protolith originated as forearc mantle

- Protolith alteration resulted from two stages of fluid-rock interaction

- First stage is due to infiltration of CO_2-rich fluid during isobaric cooling

- Second stage of fluid-rock interactions took place through prograde metamorphism

1

2

3

4

5

6   **Thermodynamic modelling of Sol Hamed serpentinite, South Eastern Desert of**

7   **Egypt: implication for fluid interaction in the Arabian-Nubian Shield ophiolites**

8

9

10   T. S. Abu-Alam[1,2] and M. M. Hamdy[1]

11

12   1 Geology Department, Faculty of Science, Tanta University, Tanta, Egypt

13   2 Institut für Erdwissenschaften, Universität Graz, Universitätsplatz 2, A-8010 GRAZ,

14   Austria

15

16   Corresponding author: T.S. Abu-Alam (tamer.abu-alam@uni-graz.at)

17

18

19

20   Short title: Fluid interaction in the Arabian-Nubian Shield ophiolites

21

22

23

24

25   **Abstract**

26

27   The Arabian-Nubian Shield is the largest tract of juvenile continental crust of the

28   Neoproterozoic. This crust was generated due to arc-arc collision associated with the

29   closing of the Mozambique Ocean, and ophiolitic rocks mark suture zones in the shield.

30   The Sol Hamed ophiolite in the southeastern Egypt defines a near-source tectonic facies,

31   representing an uncommon example of rocks that might be less deformed due to the

32   movement far from the corresponding suture. In order to understand fluid-rock

33   interactions before and during arc-arc collision, petrological, mineral chemistry, whole-

34   rock chemistry and thermodynamic studies were applied to the Sol Hamed serpentinized

35   ophiolitic mantle fragment. These studies reveal that the protolith had a harzburgite

36   composition that probably originated as forearc mantle. Protolith alteration resulted from

37   two stages of fluid-rock interaction. The first stage occurred as a result of infiltration of

38   concentrated CO_2-rich fluid released from carbonate bearing sediments and altered basalt

39   at the subduction zone. The alteration occurred during isobaric cooling at a pressure of 1

40   kbar. The fluid composition during the isobaric cooling was buffered by the metamorphic

41   reactions. The second stage of fluid-rock interactions took place through prograde

42   metamorphism. The increase in pressure during this stage occurred as a result of thrusting

43   within the oceanic crust. In this process the forearc crust was loaded by roughly 20-30 km

44   of overthrust rocks.

45

46   Key-words: Arabian-Nubian Shield; Forearc peridotite; Ophiolites; Carbonatization;

47   Thermodynamic modelling; T-XCO$_2$.

1. Introduction

Arabian-Nubian Shield (ANS) in Northeast Africa and West Arabia is the largest tract of juvenile continental crust of Neoproterozoic age on Earth (Patchett and Chase 2002; Stern et al. 2004). This crust was generated when arc terranes were created within and around the margins of the Mozambique Ocean, which formed in association with the breakup of Rodinia ~ 800–900 Ma (Stern 1994; Hassan et al. in-review). These crustal fragments collided as the Mozambique Ocean closed around 600 Ma (Meert 2003), forming arc-arc sutures, composite terranes, the Arabian-Nubian Shield (Fig. 1), and the larger collisional belt known as the East-African Orogen (Stern 1994; Kusky et al. 2003, Stern et al. 2004). Due to this collision processes a supercontinent variously referred to as Greater Gondwanaland (Stern 1994), Pannotia (Dalziel 1997) or just Gondwana (e.g. Abu-Alam et al. 2013) was formed.

Ophiolitic rocks are remarkably abundant in the ANS. They are scattered across most of the shield, over a distance of ~ 3000 km from the farthest north (Gebel Ess) almost to the equator, and from Rahib in the west to Gebel Uwayjah (45º E) in the east (Fig. 1). The abundance of the ophiolites is a further indication that the Arabian-Nubian Shield was produced by processes similar to those of modern plate tectonics (Stern et al. 2004).

The ophiolitic rocks of Eastern Desert (ED) of Egypt (Fig. 1) are interpreted to be formed in a suprasubduction zone (SSZ, e.g. Ahmed et al. 2006; Azer and Stern 2007) which operated at forearc convergent margin (e.g. Stern et al. 2004; El-Gaby 2005). The East- and West-Gondwana collision led to obduction of the SSZ ophiolitic rocks over a continental margin (Akaad and Abu El Ela 2002; El-Gaby 2005) of the West-Gondwana

70 (Abd El-Rahman et al. 2009). ~~Subduction was active while the process of ophiolitic~~

71 ~~overthrusting was operative along thrust planes (Kröner et al. 1987; Stern 1994).~~

72 The ophiolite obduction and overthrusting were associated with ~~fluid-rocks interaction~~

73 ~~and hence alteration~~, serpentinization and metasomatism ~~took place~~ (e.g. ~~Hamdy et al.~~

74 ~~2013~~) but it is often not known whether this alteration occurred before, during or after the

75 obduction (Stern et al. 2004). On other hand, much doubt exists around origin and

76 composition of the fluid during the alteration process. Some authors suggested that the

77 alteration of ultramafic rocks – the dominant component of the ANS's ophiolites –

78 occurred by interaction with hot fluid during seafloor weathering (e.g. Lebda 1995; Li

79 and Lee 2006). Other authors believed that the alteration took place by infiltration of

80 metamorphic and hydrothermal fluid along major tectonic fractures during or after rock

81 exhumation (e.g. Hyndman and Peacock 2003; Hamdy 2004; Hamdy and Lebda 2007).

82 Sol Hamed ophiolite in ~~the~~ southeastern Egypt and northeastern Sudan (Fitches et al.

83 1983) differs from other ophiolites further north in the ED of Egypt in being an elongated

84 belt defining a near-source tectonic facies (Abdelsalam and Stern 1996). To the north,

85 ophiolites occur in tectonic mélanges or as olistostromal debris, indicating a distal

86 tectonic facies. This interpretation implies the ophiolitic rocks north of the Sol Hamed

87 represent a far-travelled ophiolitic nappe, transported to the north away from its

88 corresponding suture. Thus the Sol Hamed rocks represent an uncommon example in the

89 Eastern Desert that might be less deformed by the movement along faults that occurred

90 after the closure of the Mozambique Ocean. In this work, petrological relationships,

91 mineral chemistry, geochemistry and thermodynamic modelling are described and

92 applied to rocks from Sol Hamed ophiolite (Fig. 2). The results help to more clearly

93   define the nature of the fluid-rock interactions process occurred in the intraoceanic

94   collision of the ANS.

95

96   **2. Geological setting**

97   Many of the ultramafic outcrops in the Arabian-Nubian Shield are detached, scattered

98   and isolated (Fig. 1) due to intrusion of syn- and post-tectonic plutons. Gass (1977) noted

99   that these ultramafic bodies have tectonic contacts with other Pan-African rocks. Some of

100   these ultramafic are recognized as ophiolites, representing obducted fragments of an

101   oceanic lithosphere that existed between the Proterozoic island arcs (Garson and

102   Shalaby 1976; El-Ramly et al. 1993). Dixon (1979) estimated that the ultramafic bodies

103   account for 5.3% of all Precambrian outcrops in Egypt. Serpentinized ultramafics

104   constitute the major part of these ophiolite complexes (Ahmed et al. 2001).

105   The Sol Hamed ophiolite is a part of Allaqi-Heiani-Onib-Sol Hamed-Yanbu arc-arc

106   suture (Abdelsalam and Stern 1996; Abdelsalam et al. 2003). This arc-arc suture is

107   considered − along with the Ariab-Nakasib-Thurwah-Bir Umq suture farther south in

108   Arabia and Sudan (Johnson et al. 2004) to be one of the two longest and most complete

109   Neoproterozoic ophiolite-decorated sutures in the ANS (Azer et al. 2013). Stern et al.

110   (1990) proposed that the Allaqi-Heiani-Onib-Sol Hamed-Yanbu suture represents a south

111   verging nappe which was refolded around a subhorizontal east-west trending axes to

112   produce upright antiforms and late-stage southeast verging thrusts. Vergence of the

113   ophiolite nappe was used to infer a north dipping subduction zone along the line of a

114   suture which lies north of the Allaqi-Heiani-Onib-Sol Hamed-Yanbu ophiolite. Ali et al.

115   (2010) suggested two stages for the evolution of Allaqi-Heiani-Onib-Sol Hamed-Yanbu

116   suture (~810–780 Ma and ~750–730 Ma).

117   The ultramafic rocks of Sol Hamed (Fig. 2) are composed of serpentinized peridotite

118   forming the base of a dismembered ophiolitic sequence that comprises also metagabbros,

119   pillow lavas and pelagic sediments (Abu El-Laban 2002). They occur as sheets and lenses

120   enclosed within mélange matrix comprises island arc volcanosedimentary assemblages,

121   gneiss and syn- to post-orogenic intrusions (e.g. Kröner et al. 1987; Greiling et al. 1988;

122   Taylor et al. 1993; Abd El-Naby and Frisch 2002; Kusky and Ramadan 2002;

123   Abdelsalam et al. 2003; Zoheir and Klemm 2007; Ali et al. 2010). Serpentinized

124   ophiolitic peridotites form ridges about 20 km long and about 0.4–1.8 km wide, elongated

125   in NE-SW direction. They are mostly massive but are sometimes brecciated and

126   fragmented along their contacts with the mélange matrix. Some portions contain relicts of

127   primary minerals and others are extremely altered, especially along thrusts and shear

128   zones, with the development of talc, talc-carbonate and reddish brown quartz-carbonate

129   rock (listwaenite).

130   Chromitite deposits occur mainly as lenticular bodies of variable dimensions up to 25 m

131   length × 6 m width, trending ENE-WSW. Thick pods are abundant in serpentinites that

132   are mostly derived from dunite. Micro-lenses and thin planar segregations occur in the

133   serpentinized peridotite. Gradual contacts between massive ore and serpentinized dunite

134   over a meter-range are frequently observed. A typical contact shows gradation from fine-

135   grained disseminated chromite in the dunite through nodular, to massive coarse-grained

136   chromite ore. The highly deformed chromite bodies are the most abundant. Magnesite

137   veins occur in shear zones close to the eastern periphery of the serpentinite rocks. Hamdy

6

138 (2007) based on the C-O isotopes of these veins estimated that carbon was supplied from

139 both geothermal fluids (giving magnesite with δ^{13}C values from –2.06 to –4.34‰ VPDB)

140 and metamorphic carbonaceous sediments (giving magnesite with δ^{13}C values from –9.44

141 to –10 ‰ VPDB).

142

143 **3. Petrography**

144 Variable degrees of alterations are observed in the studied ultramafic rocks. Original

145 peridotite minerals have been preserved (Table 1) in partly altered peridotites. The

146 dominant serpentine mineral is lizardite, whereas chrysotile is subordinate. The lizardite

147 forms psuedomorphic mesh and bastite textures after olivine and orthopyroxene and

148 sometimes occurs as interlocking and penetrating grains (non-pseudomorphic). The

149 chrysotile occurs as cross fiber veins traversing the lizardite matrix. Serpentine minerals

150 appear to be accompanied by shedding of fine-grained magnetite, which concentrates in

151 veins cutting zoned chromite (Fig. 3a) or along relict pyroxene cleavages. Pyroxene

152 relicts occur as inclusions in anthophyllite (Fig. 3a). The anthophyllite is a common

153 replacement mineral of orthopyroxene, where it initially grows along cleavage planes and

154 eventually replaces the whole grain. Talc is not abundant in the studied serpentinites. It

155 forms fine shreds, dense fibers and medium grained flaky crystals (0.01–0.04 mm).

156 Perfect cleavage, straight extinction and high interference colours are characteristic

157 features of the talc. The talc is pseudomorphic after anthophyllite. It is homogenous and

158 commonly associated with the alteration of orthopyroxene. All serpentinite samples

159 contain zoned-chromite (Fig. 3b) and sulphide grains. Chromite occurs as disseminated

7

160 subhedral and anhedral crystals of reddish brown colour. Some chromite grains look

161 homogeneous in reflected light.

162

163 **4. Mineral chemistry**

164 Different mineral phases were examined in the Institute of Geological Sciences of Polish

165 Academy of Sciences (IGS-PAS). The electron microprobe analyses were carried out by

166 JEOL-JXA-840A scanning electron microscope equipped with Link Analytical AN-

167 1000/855 energy dispersive X-ray spectrometer. The analytical conditions were 15 kV

168 accelerating voltage and 35 nA beam current. Mineral formula and activity of the end-

169 members were calculated by AX program (http://www.esc.cam.ac.uk/research/research-

170 groups/holland/ax). The chemical formula of the serpentine minerals was calculated

171 based on 28 oxygen atoms and ignoring the H_2O, pyroxene formula based on 6 oxygen

172 atoms. 11 oxygen atoms and ignoring the H_2O were used to calculate talc formula, 24

173 oxygen atoms were used for the spinel while the carbonate formula was calculated based

174 on 2 cations. The mineral abbreviations which will be used in the following sections are

175 from Holland and Powell (2011).

176 CaO content is below 0.03 wt% in the orthopyroxene and FeO content is in the range of

177 4.85 – 5.09 wt% while MgO content is around 35 wt% (Table 2). This reveals that the

178 main pyroxene end-member is enstatite. SiO_2 content of the serpentine ranges between

179 40.62 and 44.54 (Table 2). Al_2O_3 is in the range of below the detection limit up to 1.79

180 wt%. FeO shows a wide range (0.83 – 6.21 wt%). MgO ranges between 34.37 to 39.35

181 wt%. The MgO and the FeO ranges indicate ionic substitution between Fe^{2+} and Mg^{2+}.

182 Figure 4a shows limitation of the substitution between Al^{3+}, Mg^{2+} and Si^{4+} in the

8

183   serpentine crystals. FeO and Cr_2O_3 contents in lizardite increase (0.94 to 6.21 wt% and

184   from below detection limit to 0.36 wt% for FeO and Cr_2O_3, respectively) distinctly with

185   increasing degree of alteration from partly to completely serpentinized rocks (Table 2).

186   Chrysotile shows that Al and Cr are relatively immobile during recrystallization of

187   lizardite and therefore remain in their original crystal lattice.

188   Low Al_2O_3 and TiO_2 contents in talc chemistry reveal limitation in substitution between

189   Si, Ti and Al. The main ionic substitution is between Mg^{2+} and Fe^{2+} (Table 3). The

190   activities of talc and Fe-talc end-members are in the range of 0.68-0.85 and 0.00013-

191   0.00061, respectively. Table (4) shows chemical analyses of the carbonate minerals. The

192   high concentrations of MgO and FeO (35.53-40.14 and 8.46-14.1 wt%, respectively)

193   indicate high activity of the magnesite and the siderite end-members. The CaO content is

194   in the range of 0.04 to 0.27 wt% revealing low activity of the calcite.

195   Three compositional zones are distinguished for the spinel minerals. The composition of

196   core, intermediate and rim zones is given in Table (5) and plotted in Al-Cr-Fe^{3+} triangle

197   of Stevens (1944) (Fig. 4b). Cores and intermediates zones have aluminian chromite to

198   ferritchromite composition. Composition of the outer rim is Cr-magnetite which is nearly

199   devoid of Al and lie along the Cr–Fe^{3+} sideline (Fig. 4b). The studied spinels show

200   metamorphic conditions correspond to that of the upper greenshist to the transitional

201   greenschist-amphibolite facies (Fig. 4b).

202   The variation in the spinel composition can be interpreted as a result of chemical

203   alteration under hydrothermal conditions (Abzalov 1998; Barnes 2000; Proenza et al.

204   2004). The alteration is accompanied by decrease in Al, Mg and Cr contents and

205   consequence increase in Fe^{3+} and Fe^{2+}. Apparently with the increasing of the alteration,

9

206   Fe releases from olivine and orthopyroxene and Cr releases from chromite and are

207   accommodated in the serpentines. In addition, the wide compositional variation

208   (particularly in Al_2O_3) reflects temporal and/or spatial variations in melt types (boninitic

209   and tholeiitic) that were generated from, and emplaced in subarc mantle domains in a

210   suprasubduction zone environment (Hamdy and Lebda 2011).

211

212   **5. Whole-rock chemistry**

213   Representative bulk rock chemistry of Sol Hamed serpentinite is given in Table (6).

214   Chemical analyses of major and some trace elements were carried out at the

215   geochemistry labortory of the IGS-PAS. Concentrations of major and trace elements were

216   determined after microwave-assisted acid digestion with atomic absorption

217   spectrophotometer (AAS-PU 9100xUNICAM). Before digestion samples were heated to

218   1100 to determine loss on ignition (LOI). Analytical precession was better than 0.5% for

219   major elements and 4 ppm for trace elements.

220   Due to the almost complete serpentinization of some of the Sol Hamed peridotites, modal

221   compositions could not be determined. Therefore, normative compositions were

222   calculated from anhydrous analyses using the CIPW norm, assuming a Fe_2O_3/FeO ratio

223   of 0.2 (Melcher et al. 2002), and plotted in Streckeisen (1976) classification diagram (not

224   shown). The normative contents of olivine, orthopyroxene, and clinopyroxene of the

225   studied Sol Hamed serpentinites classify them as harzburgites. Trace element values are

226   typical of residual mantle (e.g. high Cr (2.696–2.742 ppm), Ni (1.650–2.381 ppm) and Co

227   (116.20-166.79 ppm)). In contrast, the contents of Ba, Pb, Sr and, Li are highly

228   concentrated compare to depleted and pristine mantle peridotites (McDonough and Sun

10

229 1995). This enrichment in the fluid-mobile elements may be directly related to the

230 serpentinization process or due to metasomatism by subduction-related fluids (Hamdy et

231 al. 2013).

232

233

234 **6. Discussion**

235 *6.1. Origin and tectonic setting of the serpentinite protolith*

236 Earth contains two main shallow mantle domains: sub-oceanic lithosphere and sub-

237 continental lithosphere. The Sol Hamed harzburgite falls within the oceanic array (Niu

238 2004) in $MgO/SiO_2–Al_2O_3/SiO_2$ space (Fig. 5). The oceanic array is parallel to the

239 terrestrial array but offset to lower MgO/SiO_2 values, presumably due to loss of MgO

240 during low-temperature seafloor weathering and not due to the serpentinization process

241 itself (Snow and Dick 1995; Niu 2004). Oceanic peridotites may originate in a variety of

242 tectonic environments including mid-ocean ridge (MOR), suprasubduction zone (SSZ)

243 and rifted margins settings. We term these suprasubduction zone (SSZ) peridotites

244 (Pearce et al. 1984); a group that incorporates peridotites from both island arcs and

245 spreading centers above subduction zones. These discrete genetic types are distinct in

246 mineralogical and geochemical characteristics of mantle residues. Composition of the

247 unaltered accessory spinel is extensively used as a petrogenetic and geotectonic indicator

248 (e.g. Barnes and Roeder 2001). Chromium numbers $[Cr/(Cr+Fe^{3+}+Al)]$ higher than 0.6

249 are usually restricted to subduction-related rocks (Dick and Bullen 1984). Ishii et al.

250 (1992) used the Mg# $[Mg/(Mg+Fe^{2+})]$ and Cr# of the spinel to discriminate between

251 peridotites from MOR, forearc and back-arc settings. Spinels from the Sol Hamed

252 serpentinites lie in the chemical space of the forearc peridotite (Fig.6) and distinctly

253 higher than spinels from MOR and back-arc basin in the Cr#. This indicates that the Sol

254 Hamed serpentinites represent a fragment of oceanic lithosphere that has been

255 incorporated above subduction zone in a forearc.

256 Hellebrand et al. (2001) tested which trace elements correlate with major element

257 indicators of partial melting in central Indian ridge peridotites. The most common of

258 these is the Cr# in spinel. They found a well-defined correlation between moderately

259 incompatible elements, such as HREEs in clinopyroxene with spinel Cr#. Hellebrand et

260 al. (2001) developed an empirical equation ($F = 10 \ln (\text{Cr\#}) + 24$) to estimate the degree

261 of melting F (in percent) as a function of spinel Cr#. Using the equation of Hellebrand et

262 al. (2001), the estimated melting in the studied peridotites ranges from 20 to 22%.

263

264   *6.2. Thermodynamic modelling*

265 All the thermodynamic calculations in the following sections were calculated by

266 THERMOCALC (Powell and Holland 1988), PerPle_X (Connolly 1990) and using the

267 internally consistent dataset of Holland and Powell (2011). Lizardite bearing reactions

268 which were proved experimentally (i.e. liz = br atg (Evan 2004), liz = chr (Chernosky

269 1975), liz = ta fo clin H_2O (Caruso and Chernosky 1979)) will be only used (Fig. 7).

270 Figure 7 shows a *P-T* grid in the system CFMASH for the following end-members: atg,

271 chr, en, fs, di, hed, fo, fa, anth, tr, clin, ta, sp, herc, mgts, fta, br, H_2O. Activity of the H_2O

272 is imposed to be the unity therefore all the CO_2 bearing phases are not seen in this grid.

273 The *P-T* grid shows forty six univariant equilibria, five invariant points and three

274 experimental lizardite bearing reactions. All the H_2O bearing univariant reactions show

275   steep slope in the *P-T* space. Consequently these reactions can be used as temperature

276   indicators. Two water absent invariant points (508 $^{\circ}$C-1.08 kbar and 542 $^{\circ}$C-2.2 kbar)

277   involve reactions with notable change in the volume and can be used as pressure

278   indicators. For better reading to the *P-T* grid, only the interesting reactions are shown in

279   Figure 8 using two different scales for temperature axe.

280

281   *Anthophyllite and talc formation*

282   One of the key petrographic features is the relation between pyroxene, anthophyllite and

283   talc. The anthophyllite is a common replacement mineral of orthopyroxene. The

284   anthophyllite can be formed due to eight metamorphic reactions (Fig. 8), however the

285   absence of clinochlore and the formation of the talc psuedomorphic after anthophyllite

286   make the only possibility to crystallize anthophyllite is due to breakdown of high grade

287   minerals (i.e. pyroxene). Two reactions can produce anthophyllite during a retrograde

288   path at relatively high pressure (> 1.7 kbar) and above the atg-chr-fs-di-hed-fa-tr-ta-herc-

289   fta-br-mgts invariant point, however, these reactions produce clinochlore in considerable

290   values. This makes reaction fa anth=fs en H_2O and the lower pressure part (< 1.7 kbar) of

291   reaction fo anth=en H_2O are preferred way to produce anthophyllite in the assumed fluid

292   composition.

293   Eight reactions can produce talc as a retrograde phase due to breakdown of high grade

294   assemblage that includes anthophyllite. Four reactions can be excluded since they contain

295   clinochlore as a reactant or a product. The petrographic observation "orthopyroxene

296   consumed due to talc growing" makes fa ta=fs anth H_2O, ta sp=H_2O mgts anth reactions

297   (Fig. 8) are the favorable equilibria to produce talc. The two talc producing reactions

13

298   have a temperature range 630 - 790 ^{o}C in a wide pressure condition. The pressure

299   conditions of anthophyllite formation (< 1.7 kbar) make the upper temperature limit of

300   talc producing reactions is below 730 ^{o}C. Other reactions can produce anthophyllite and

301   talc in the same pressure-temperature range but with different fluid compositions, these

302   reactions will be discussed in the fluid composition section.

303   Talc and anthophyllite formations indicate isobaric cooling path at pressure below 1.7

304   kbar and in a temperature range of 800-550 ^{o}C. The cooling path can be extended to a

305   lower temperature condition based on the presence of lizardite in the studied assemblage.

306   This assumption is in agreement with the greenschist facies conditions of the intermediate

307   zone of the spinel grains (Fig. 4b).

308   Stern et al. (2004) reconstructed the ophiolitic sequence of the Arabian-Nubian Shield

309   and concluded that the ophiolitic successions have crustal thicknesses of 2.5 to 5 km.

310   These crustal thicknesses are equivalent to pressure 0.7 and 1.4 kbar, respectively (Fig. 8)

311   assuming lithostatic conditions and a rock density of 2.84 x 10^{3} kg/m^{3} (Carlson and

312   Raskin 1984). This constrains pressure conditions of the formation of the anthophyllite

313   and talc process by 0.7-1.4 kbar (the retrograde path as shown by the black arrow in

314   Figure 8).

315

316   *Chrysotile formation and prograde metamorphism*

317   Presence of chrysotile fibers traversing the lizardite matrix indicates that the rocks passed

318   the reaction liz = chr (Fig. 8). Hamdy and Lebda (2007) showed that the magnetite rims

319   of the chromite grains of Malo Grim serpentinites (part of the Sol Hamed ophiolites)

320   equilibrated at a temperature range of 500-550 ^{o}C. These conditions are in agreement

321   with the composition of the rim zones of the spinel grains which show condition of

322   amphibolite facies (Fig. 4b). Neither petrographic observations nor mineral chemistry

323   data allow predicting the pressure conditions of chrysotile formation.

324   The Arabian-Nubian shield ophiolites were obducted within volcanic arc assemblages

325   due to arc-arc collision process (e.g. Stern 1994; Kusky et al. 2003; Meert 2003; Stern et

326   al. 2004). Obducted ophiolites, associated volcanics and sediments may represent an

327   accretionary prism system. Here we will follow the assumption of Valli et al. (2004) that

328   average thermal gradient of ancient and modern accretionary prisms can be in the range

329   of 30 ^{o}C/km and 10 ^{o}C/km, respectively (Fig. 8). El-Naby and Frisch (1999) studied

330   Allaqi-Heiani ophiolite belt and they concluded that these ophiolites record temperature

331   of 700 ^{o}C and pressures up to 8 kbar. These conditions can be converted to a thermal

332   gradient of 25 ^{o}C/km which locates between the two assumed thermal gradient. This

333   thermal gradient cuts the predicted temperature (500-550 ^{o}C) in a pressure range of 5.5-

334   6.5 kbar (Fig. 8).

335

336   *Fluid composition and T-XCO_2 section*

337   Due to the ambiguity around the pressure condition during the prograde path of the

338   studied samples, the fluid composition will be studied only along the cooling path. Figure

339   9 shows a *T-X*CO_2 grid in the system CFMASH-CO_2 for the following end-members:

340   anth, atg, chr, en, fs, di, hed, fo, fa, ta, sp, herc, mgts, fta, mag, sid, H_2O, CO_2 at 1 kbar

341   (the cooling path of Figure 8). The *T-X*CO_2 grid was constructed in the full *X*CO_2 range

342   (not shown here), however all anthophyllite and talc producing invariant points occur at

343   high $X CO_2$ (> 0.88). In this type of sectioning (*P-, T-X*CO_2)*, mineral phases are produced

15

344 mainly at the invariant point conditions (Spear 1993). The grid includes twenty five

345 univariant reactions and seven invariant points. All of these invariant points occur at

346 temperature range of 450-520 $^{\circ}$C (Fig. 9). All the invariant points above 500 $^{\circ}$C are

347 magnesite-siderite absent invariant points. At 500 $^{\circ}$C and XCO$_2$ (0.913), magnesite-

348 bearing invariant point appears. With cooling, the carbonate phase (siderite) becomes

349 more stable (at 460 $^{\circ}$C and XCO$_2$ (0.978)). Below 450 $^{\circ}$C, the magnesite becomes

350 metastable (Fig. 9). These invariant points show sequence of fluid evolution in the Sol

351 Hamed serpentinites.

352 At XCO$_2$ range (0.88-0.99), the first talc producing reaction (ta sp=mgts anth H$_2$O (Fig.

353 9)) is at higher temperature than any anthophyllite producing reactions which were

354 discussed in the P-T grid. Consequently reaction (herc anth=mgts en fs H$_2$O) is the

355 preferred anthophyllite producing reaction. Once the rocks started the cooling path, the

356 anthophyllite producing reaction (op. cit.) buffers the fluid composition of the system and

357 the T-XCO$_2$ path (dashed arrows in Figure 9) followed the reaction till the mineral

358 composition arrives the atg-chr-di-hed-fo-fa-sp-fta-mag-sid-CO$_2$ invariant point (510 $^{\circ}$C;

359 0.998 (XCO$_2$)). The assemblage stayed at the invariant point conditions until one of the

360 phases (i.e. fs, herc, mgts) was completely consumed or excluded out the equilibrium. At

361 this stage of the path, the rocks follow the isothermal reaction (ta en=anth H$_2$O) which

362 produces a considerable amount of talc. This reaction crosses all the invariant points at

363 510 $^{\circ}$C with different XCO$_2$ composition (Fig. 9). Presence of magnesite in the studied

364 assemblage (Table 4) and presence of magnesite-bearing invariant point at 500 $^{\circ}$C and

365 XCO$_2$ (0.913) make the only possibility to terminate the talc producing reaction (op. cit.)

366 is at the atg-chr-fs-di-hed-fa-sp-herc-mgts-fta-mag-sid-CO$_2$ invariant point (510 $^{\circ}$C;

367   0.885 (XCO_2)). The assemblage stayed at this invariant point until the anthophyllite was

368   trapped and excluded out the equilibrium, afterward the mineral equilibrium follows the

369   reaction (fo ta=en H_2O) until the magnesite-bearing invariant point at 500 ^{o}C and XCO_2

370   (0.913) which allows the first appearance of carbonate-bearing phase. Forsterite

371   consuming drives the equilibrium to leave the magnesite-bearing invariant point toward

372   the magnesite-siderite-bearing invariant point (460 ^{o}C and XCO_2 (0.978)). Subsequently

373   the reaction (ta sid=en fa CO_2 H_2O) buffers the equilibrium until the magnesite becomes

374   metastable at 450 ^{o}C and 0.984 (XCO_2). Finally, reaction (ta sid=en fs CO_2 H_2O)

375   produces talc and siderite with constant consuming rate of H_2O and CO_2.

376

377   *6.3. Fluid source and Tectonic implications*

378   Decarbonation of altered metabasalts and carbonates of marine sediments at low pressure

379   condition has been considered as a possible mechanism in order to explain CO_2 fluxes at

380   convergent margins (Staudigel et al. 1996; Kerrick and Connolly 1998; Fischer et al.

381   1998; Molina and Poli 2000). When hot geotherms are assumed, CO_2-rich fluids can be

382   transferred from the altered oceanic crust to shallower reservoirs (Fig. 10) in the forearc

383   region (Molina and Poli 2000). This mechanism can account for the CO_2 enrichment of

384   lithospheric mantle on a long-term scale and it may explain the occurrence of carbonates

385   in peridotite xenoliths (Ionov et al. 1993) as well as in some camptonitic lamprophyres

386   (Bea et al. 1999). Here this mechanism can be used to explain the high CO_2 fluxes in the

387   studied ophiolites (XCO_2 = 0.89-0.99 (Fig. 9)). This high CO_2 fluid content reacted with

388   the ophiolitic rocks in the forearc (Fig. 10) under pressure condition of 1 kbar and

389   temperature of around 800 ^{o}C (Fig. 8). Stern and Gwinn (1990) argued on the basis of C

390 and Sr isotopic that carbonate intrusions in the Eastern Desert of Egypt - which could be

391 related to the carbonatizing fluids affecting Arabian-Nubian Shield ultramafic rocks - are

392 mixtures of mantle derived and remobilized sedimentary carbonate. Hamdy and Lebda

393 (2007) concluded the same conclusion based on carbon isotope composition of south

394 Eastern Desert of Egypt.

395 T-XCO$_2$ grid (Fig. 9) shows that the fluid composition was buffered all the time by the

396 metamorphic reactions (e.g. Greenwood 1975; Rice and Ferry 1982; Spear 1993; Abu-

397 Alam et al. 2010). Field, petrographical and mineral chemistry evidences support this

398 thermodynamic observation. Majority of the T-XCO$_2$ path took place at a temperature

399 range of 450 – 550 ^{o}C. Most of the reactions in this range of the temperature occurred as

400 isothermal reactions which means that the rocks were held at this temperature for a time

401 period enough to consume one phase or more to drive the equilibria toward a lower

402 temperature conditions. Figure 5a of Hamdy and Lebda (2007) shows that spinel minerals

403 of the studied ophiolites were re-equilibrated at temperature condition of 500-550 ^{o}C

404 which is the same range provided by the T-XCO$_2$ grid. Presence of magnesite in

405 considerable amount in thin-section scale as well as presence of small pockets and veins

406 of magnesite in outcrop scale, indicate that the rocks were held for a long time at the two

407 magnesite-bearing invariant points (at temperature 500 and 460 ^{o}C (Fig. 9)).

408 The high pressure condition (8 kbar) which was assumed by El-Naby and Frisch (1999)

409 and which was used here to predict the geothermal gradient and the prograde path (the

410 black arrow of Figure 8) as well the predicted pressure range (5.5-6.5 kbar from this

411 study) can be explained in the context of extensive duplex array and thickness of the

412 original ophiolitic sequence (e.g. Hirono and Ogawa 1998; Ueno et al. 2011). Oceanic

413   crust in a forearc setting can be overloaded by obduction of a crust that formed in a mid-

414   oceanic ridge and the thrusting in the forearc crust itself can add more loads (Fig. 10).

415   Original thickness of the Arabian-Nubian Shield's ophiolitic sequence is 2.5 to 5 km

416   (Stern et al. 2004). Following oceanic crust density of 2.84 x 10^3 kg/m^3 (Carlson and

417   Raskin 1984), the studied ophiolites were overloaded by 20-28 km thickness of obducted

418   and thrusted oceanic crust from both mid-oceanic and forearc settings. This is in

419   agreement with thickness of the original sequence by a factor in range of 5.6 and 11.2.

420   The same thickening factors were suggested numerically by Ueno et al. (2011).

421   One of the opened questions around the ophiolites of the Arabian-Nubian Shield is "*when*

422   *did the alteration take place? Is it before or after the obduction?* (Stern et al. 2004)".

423   Clearly, petrographic observations and thermodynamic modelling that are presented here

424   give an answer to this question. The studied ophiolites show two segments of the *P-T*

425   path; one is the isobaric cooling path at pressure condition of 1 kbar and the second is

426   prograde path from a pressure 1 kbar up to 5.5-6.5 kbar (black arrow of Figure 8). The

427   isobaric cooling path occurred under oceanic crustal thickness of 3.5 km which means

428   that the first stage of alteration took place before the obduction while the second stage

429   occurred during thrusting and obduction processes (prograde metamorphism). At today

430   situation, the ophiolites are thrusted over volcanic arc-assemblage. The volcanic arc-

431   assemblage of the Arabian-Nubian Shield records a peak pressure around 3-4 kbar (e.g.

432   Noweir et al. 2006; Abu-Alam 2005; Abu-Alam and Farahat unpublished data). This can

433   be ensued only if the ophiolites achieved the peak condition (5.5-6.5 kbar) before the

434   final thrusting above the low-pressure arc-assemblage.

435

19

7. Conclusions

The Sol Hamed serpentinised ophiolitic mantle peridotite in the south Eastern Desert of Egypt at the Allaqi-Heiani-Onib-Sol Hamed-Yanbu arc-arc suture formed in forearc setting and later thrusted over low-grade arc-assemblage of the Arabian-Nubian Shield. It shows a *P-T* path of an isobaric cooling at lithostatic pressure of 1 kbar which is equivalent to an oceanic crustal thickness of 3.5 km. The alteration occurred before the thrusting and at high CO_2 fluxes. The decarbonation of altered oceanic metabasalts and carbonates of marine sediments at low pressure condition can be considered as a possible mechanism to explain the high concentrated CO_2 fluid fluxes at the convergent margin. The concentration of the fluid during the cooling path was buffered by the metamorphic reactions. The second segment of the path represents a prograde metamorphism which occurred under extensive duplex array and thrust pp of the oceanic crust. The crust in the forearc basin was overloaded by 20-28 km of obducted and thrusted oceanic crust from both mid-oceanic and forearc basin. This is equivalent to thickness of the original ophiolitic sequence by a factor in range of 5.6 and 11.2.

461 **References**

462 Abd El-Naby HH, Frisch W (2002) Origin of the Wadi Haimur-Abu Swayel gneiss belt,
463   south Eastern Desert, Egypt: Petrological and geochronological constraints.
464   Precamb Res 113:307–322.

465 Abd El-Rahman Y, Polat A, Dilek Y, Fryer BJ, El-Sharkawy M, Sakran S (2009)
466   Geochemistry and tectonic evolution of the Neoproterozoic incipient arc-forearc
467   crust in the Fawakhir area, Central Eastern Desert of Egypt. Precambrian Res
468   175:116–134.

469 Abdelsalam MG, Stern RJ (1993) Tectonic evolution of the Nakasib suture, Red Sea
470   Hills, Sudan: evidence for a late Precambrian Wilson Cycle. J Geol Soc 150:
471   393-404.

472 Abdelsalam MG, Stern RJ (1996) Sutures and shear zones in the Arabian-Nubian Shield.
473   J Afr Earth Sci 23: 289–310.

474 Abdelsalam MG, Abdeen MM, Dowaidar HM (2003) Structural evolution of the
475   Neoproterozoic Western Allaqi-Heiani suture, southeastern Egypt. Precambrian
476   Res 124: 87-104.

477 Abu-Alam TS (2005) Geological studies of the area around Wadi Kareim, Central
478   Eastern Desert, Egypt. M.Sc., Tanta University.

479 Abu-Alam TS, Santosh M, Brown M, Stüwe K (2013) Gondwana Collision. Miner Petrol
480   DOI 10.1007/s00710-013-0283-5

481 Abu-Alam TS, Stüwe K, Hauzenberger C (2010) Calc-silicates from Wadi Solaf region,
482   Sinai, Egypt. J Afr Earth Sci 58: 475–488.

483 Abu El Laban SA (2002) Some geological and geochemical studies in Abu Ramad Area,
484   South Eastern Desert, Egypt. PhD. Cairo University. p. 274.

485 Abzalov MZ (1998) Chrome-spinels in gabbro-wherlites intrusions of the Pechenga area,
486   Kola Peninsula, Russia: emphasis on the alteration features. Lithos 43: 109-134.

487   Ahmed AH, Arai S, Attia AK (2001) Petrological characteristics of podiform chromitites
488   and associated peridotites of Pan-African complexes of Egypt. Mineralium
489   Depos 36:72–84.

490   Ahmed AH, Hanghøj K, Kelemen PB, Hart SR, Arai S (2006) Osmium isotope
491   systematics of the Proterozoic and Phanerozoic ophiolitic chromitites: in situ ion
492   probe analysis of primary Os-rich PGM. Earth Planet Sci Lett 245:777–791.

493   Akaad MK, Abu El Ela AM (2002) Geology of the basement rocks in the eastern half of
494   the belt between latitudes 25º 30' and 26º 30'N Central Eastern Desert, Egypt.
495   Geological Survey of Egypt, Paper No. 78. 118p.

496   Ali KA, Azer MK, Gahlan HA, Wilde SA, Samuel MD, Stern RJ (2010) Age of
497   formation and emplacement of Neoproterozoic ophiolites and related rocks
498   along the Allaqi Suture, south Eastern Desert, Egypt. Gond Res 18:583–595.

499   Azer MK, Stern RJ (2007) Neoproterozoic (835-720 Ma) serpentinites in the Eastern
500   Desert, Egypt: Fragments of Fore-arc mantle. J Geol 15:457–472.

501   Azer MK, Samuel MD, Gahlan HA, Stern RJ, Ren M, Moussa HE (2013) Neoproterozoic
502   ophiolitic peridotites along the Allaqi-Heiani suture, South Eastern Desert,
503   Egypt. Miner Petrol DOI 10.1007/s00710-012-0204-z

504   Barnes SJ (2000) Chromite in komatiites, II. Modifications during greenschist to mid-
505   amphibolite facies metamorphism. J. Petrol., 41: 387-409.

506   Barnes SJ, Roeder PL (2001) The Range of Spinel Compositions in Terrestrial Mafic and
507   Ultramafic Rocks. J Petro 42: 2279–2302.

508   Bea F, Monetero P, Molina JF (1999) Mafic precursors, peraluminous granitoids, and late
509   lamprophyres in the Avila batholith: a model for the generation of Variscan
510   batholiths in Iberia. J Geol 107: 399-419.

511   Bloomer SH, Taylor B, MacLeod CJ, Stern RJ, Fryer P, Hawkins JW, Johnson L (1995)
512   Early Arc Volcanism and the Ophiolite Problem: A Perspective from Drilling in
513   the Western Pacific. In: Taylor B, Natland J (Eds.) Active Margins and Marginal
514   Basins of the Western Pacific. American Geophysical Union, Washington, DC,
515   pp 1–30.

516   Carlson RL, Raskin GS (1984) Density of the ocean crust. Nature 311: 555-558.

517   Caruso LJ, Chernosky JV (1979) The stability of lizardite. Can Mineral 17: 757-769.

518   Chernosky JV (1975) Aggregate refractive indices and unit-cell parameters of synthetic
519   serpentine in the system $MgO-Al_2O_2-SiO_2-H_2O$. Ameri Minera. 60: 200-208.

520   Connolly JAD (1990) Multivariable phase-diagrams - an algorithm based on generalized
521   thermodynamics. Amer J Sci 290: 666-718.

522   Dalziel IWD (1997) Neoproterozoic-Paleozoic geography and tectonics: Review,
523   hypothesis, environmental speculation. Geol Soc Ameri Bull 109: 16–42.

524   Dick HJB, Bullen T (1984) Chromian spinel as a petrogenetic indicator in abyssal and
525   Alpine-type peridotites and spatially associated lavas. Contrib Mineral Petrol
526   86:54–76.

527   Dixon TH (1979) The evolution of continental crust in the Late Precambrian
528   Egyptian Shield. PhD Thesis, Univ California.

529   El-Gaby S (2005) Integrated evolution and rock classification of the Pan-African belt in
530   Egypt. First Symposium on the Classification of the Basement Complex of
531   Egypt, pp. 1-9.

532   El-Naby HA, FrischW, (1999) Metamorphic sole of Wadi Haimur-Abu Swayel ophiolite:
533   Implications on late Proterozoic accretion. In: Wall HD, Greiling RO (Eds.),
534   Aspects of Pan-African Tectonics. Heidelberg, Germany, pp 9–14.

535   El-Ramly MF, Greiling RO, Rashwan AA, Rasmy AH (1993) Explanatory note
536   to accompany the geological and structural maps of Wadi Hafafit area,
537   Eastern Desert of Egypt. Geol Surv Egypt 68: 1-53

538   Evans BW (2004) The serpentinite multisystem revisited: Chrysotile is metastable. Inter
539   Geol Rev 46:479–506.

540   Evans BW, Frost, BR (1975) Chrome-spinel in progressive metamorphism – a
541   preliminary analysis. Geochim Cosmochim Acta 39: 959–972.

542 Fischer TP, Giggenbach WF, Sano Y, Williams SN (1998) Fluxes and sources of
543   volatiles discharged from Kudryavy, a subduction zone volcano, Kurile Island.
544   Earth Planet Sci Lett 160: 81-96.

545 Fitches W, Graham R, Hussein I, Ries A, Shackleton R, Price R (1983) The late
546   Proterozoic ophiolite of Sol Hamed, NE Sudan. Precambrian Res 19:385-411.

547 Garson MS, Shalaby IM (1976) Precambrian-Lower Palaeozoic plate tectonics
548   and metagabbros in the Red Sea region. Spec Pap Geol Assoc Can 14:
549   573-596.

550 Gass IG (1977) The evolution of the Pan African crystalline basement in NE
551   Africa and Saudi Arabia. J Geol Soc Lond 134: 129-138.

552 Greenwood HJ (1975) Buffering of pore fluids by metamorphic reactions. Ameri J Sci
553   275: 573-593.

554 Greiling RO, Kröner A, El Ramly MF, Rashwan AA (1988) Structural relationships
555   between the southern and central parts of the Eastern Desert of Egypt: details of
556   a fold and thrust belt. In: El Gaby S, Greiling RO (eds) The Pan-African Belt of
557   Northeast Africa and adjacent areas. Vieweg and Sohn, Weisbaden, pp 121–145

558 Hamdy MM (2004) Continental upper mantle in the area of the Sudetes on the basis of
559   mineralogical and geochemical studies of ultramafic rock occurrences, SW
560   Poland. PhD Thesis, Institute of Geological Sciences, Polish Academy of
561   Sciences, 221p.

562 Hamdy MM (2007): Stable isotope and trace element characteristics of some
563   serpentinite-hosted vein magnesite deposits from the Eastern Desert of Egypt:
564   arguments for magmatism and metamorphism-related mineralising fluids.
565   M.E.R.C. Bulletin, 21, 29-50.

566 Hamdy MM, Lebda EM (2007) Metamorphism of ultramafic rocks at Gebel Arais and
567   Gebel Malo Grim, Eastern Desert, Egypt: mineralogical and O–H stable isotopic
568   constraints. Egypt J Geol 51: 105-124.

25

569 Hamdy MM, Lebda EM (2011) Al-compositional variation in ophiolitic chromitites from
570   the south Eastern Desert of Egypt: Petrogenetic implications. J Geol Min Res 3:
571   232-250.

572 Hamdy MM, Harraz HZ, Aly GA (2013) Pan-African (intraplate and subduction-
573   related?) metasomatism in the Fawakhir ophiolitic serpentinites, Central Eastern
574   Desert of Egypt: mineralogical and geochemical evidences. Arab J Geosci, 6,
575   13-33, DOI 10.1007/s12517-011-0319-2.

576 Hart SR, Zindler A (1986) In search of a bulk-Earth composition. Chem Geol 57: 247-
577   267.

578 Hellebrand E, Snow JE, Dick HJB, Hofmann AW (2001) Coupled major and trace elements as
579   indicators of the extent of melting in mid-ocean-ridge peridotites. Nature 410: 677–681.

580 Hirono T, Ogawa Y (1998): Duplex arrays and thickening of accretionary prisms: An example
581   from Boso Peninsula, Japan. Geol 26: 779-782.

582 Holland TJB, Powell R (2011) An improved and extended internally consistent thermodynamic
583   dataset for phases of petrological interest, involving a new equation of state for solids. J
584   Meta Geol 29: 333-383.

585 Hyndman RD, Peacock SM (2003) Serpentinization of the forearc mantle. Earth Planet
586   Sci Lett 212: 417-432.

587   Ionov DA, Dupuy C, O'Reilly SY, Kopylova MG, Genshaft YS (1993) Carbonated
588   peridotite xenoliths from Spitspergen: implications for trace element signature of
589   mantle carbonate metasomatism. Earth Planet Sci Lett 119: 283-297.

590 Ishii T, Robinson PT, Maekawa H, Fiske R (1992) Petrological studies of peridotites
591   from diapiric serpentinite seamounts in the Izu-Ogasawara-Mariana forearc. In:
592   Fryer P, Pearce JA, Stokking LB (eds.) Proceedings of the Ocean Drilling
593   Program Scientific Results 125. Ocean Drilling Program, College Station, TX,
594   pp 445–485.

595 Johnson PR, Kattan FH, Al-Saleh AM (2004) Neoproterozoic ophiolites in the Arabian
596   Shield. In: Kusky TM (ed) Precambrian ophiolites and related rocks. In:
597   Developments in precambrian geology 13, Elsevier, 129–162

598   Kerrick DM, Connolly JAD (1998) Subduction of ophicarbonates and recycling of CO_2
599   and H_2O. Geology 26: 375-378.

600   Kröner A, Greiling RO, Reischmann T, Hussein IM, Stern RJ, Durr S, Kruger J, Zimmer
601   M (1987) Pan-African crustal evolution in the Nubian segment of northeast
602   Africa. In: Kröner A (ed) Proterozoic lithospheric evolution. American
603   Geophysical Union, Geodynamics Series 17: 237-257.

604   Kusky TM, Ramadan TM (2002) Structural controls on Neoproterozoic mineralization in
605   the South Eastern Desert, Egypt: an integrated field, Landsat TM, and SIR-C/X
606   SAR approach. J Afr Earth Sci 35:107–121

607   Kusky TM, Abdelsalam M, Tucker R, Stern R (2003) Evolution of the East African and
608   Related Orogens, and the Assembly of Gondwana. Special Issue of Precambrian
609   Res 123: 81–344.

610   Lebda, E.M., 1995, Petrology and mineral chemistry of serpentinite rocks of the
611   Gogołów-Jordanów massif, SW Poland. Ph.D. Thesis, Wrocław University,
612   Poland, 189p.

613   Li Z-X A, Lee C-T A (2006) Geochemical investigation of serpentinized oceanic
614   lithospheric mantle in the Feather River Ophiolite, California: Implications for
615   the recycling rate of water by subduction. Chem Geol 235: 161-185.

616   McDonough WF, Sun SS (1995) Composition of the Earth. Chem Geol 120: 223-253.

617   Meert, JG (2003) A synopsis of events related to the assembly of eastern Gondwana.
618   Tectonophy 362, 1–40.

619   Melcher F, Meisel T, Puhl J, Koller F (2002) Petrogenesis and geotectonic setting of
620   ultramafic rocks in the Eastern Alps: constraints from geochemistry. Lithos 65:
621   69-112.

622   Molina JF, Poli S (2000) Carbonate stability and fluid composition in subducted oceanic
623   crust: an experimental study on H_2O-CO_2-bearing basalts. Earth Planet Sci
624   Lett176: 295-310.

625   Niu YL (2004) Bulk-rock major and trace element compositions of abyssal peridotites:
626   Implications for mantle melting, melt extraction and post-melting processes
627   beneath ocean ridges. J Petro 45: 2423-2458.

628   Noweir MA, Ghoneim MF, Abu-Alam TS (2006) Deformational phases and tectonic
629   evolution of the Neoproterozoic rocks of Wadi Kareim area, Central Eastern
630   Desert, Egypt. Annals J. Geol. Surv., 28, 81-109.

631   Patchett PJ, Chase CG (2002) Role of transform continental margins in major crustal
632   growth episodes. Geology 30: 39–42.

633   Pearce JA, Lippard SJ, Roberts S (1984) Characteristics and tectonic significance of
634   suprasubduction zone ophiolites. In: Kokelaar BP, Howell MF (Eds) Marginal
635   Basin Geology. Geological Society of London, pp. 77–94.

636   Powell R, Holland TJB (1988) An internally consistent thermodynamic dataset with
637   uncertainties and correlations: 3. Application, methods, work examples and a
638   computer program. J Meta Geol 6: 173-204.

639   Proenza JA, Ortega-Gutiérrez F, Camprubí A, Tritlla J, Elías-Herrera M, Reyes-Salas M
640   (2004) Paleozoic serpentinite-enclosed chromitites from Tehuitzingo (Acatlán
641   Complex, southern Mexico): a petrological and mineralogical study. J. S. Am.
642   Earth Sci., 16: 649-666.

643   Purvis AC, Nesbitt RW, Halberg JA (1972) The geology of part of Carr Boyd Complex
644   and its associated nickel mineralization, Western Australia. Econ Geol 67:
645   1093-1113.

646   Rice JM, Ferry JM (1982) Buffering, infiltration and the control of intensive variables
647   during metamorphism. In: Ferry JM, Characterization of Metamorphism through
648   Mineral Equilibria. Reviews in Mineralogy, 10, Mineralogical Society of
649   America, Washington, D. C. pp 263-326.

650   Snow JE, Dick HJB (1995) Pervasive Magnesium Loss by Marine Weathering of
651   Peridotite. Geochim. Cosmochim. Acta 59: 4219-4235.

652   Spear FS (1993) Metamorphic phase equilibria and pressure-temperature-time paths.
653   Mineralogical Society of America, USA.

654 Staudigel H, Plank T, White B, Schmincke HU (1996) Geochemical fluxes during
655   seafloor alteration of the basaltic upper oceanic crust DSDP Site 417 and 418,
656   AGU Geo phys Monogr 96: 19-37.

657 Stern R (1994) Arc assembly and continental collision in the neoproterozoic east African
658   orogen: implications for the consolidation of Gondwana. Ann Rev Earth Planet
659   Sci Lett 152:75–91.

660 Stern RJ, Gwinn CJ (1990) Origin of late precambrian intrusive carbonates, Eastern
661   Desert of Egypt and Sudan: C, O and Sr isotopic evidences. Precam Res 46:259–
662   272.

663 Stern R, Johnson PR, Kröner A, Yibas B (2004) Neoproterozoic ophiolites of the
664   Arabian–Nubian Shield. In: Kusky TM (ed) Precambrian ophiolites and related
665   rocks. Developments in Precambrian geology, vol 13. Elsevier, Amsterdam, pp
666   95–128.

667 Stern R, Nielsen K, Best E, Sultan M, Arvidson R, Kröner A (1990) Orientation of late
668   Precambrian sutures in the Arabian-Nubian shield. Geology 18: 1103–1106.

669 Stevens, R. E., 1944, Composition of some chromites of the Western Hemisphere. Ameri
670   Minera. 29, 1-34.

671 Streckeisen A (1976) Classification of the common igneous rocks by means of their
672   chemical composition. A provisional attempt. Neues Jahr Buch für Mineralogie,
673   1: 1-15.

674 Suita MTF, Strieder AJ (1996) Cr-spinel from Brazilian mafic-ultramafic complexes:
675   metamorphic modifications. Int Geol Rev 38: 245-267.

676 Taylor WEG, El Kazzaz YAH, Rashwan AA (1993) An outline of the tectonic
677   framework for the Pan-African orogeny in the vicinity of Wadi Um Relan area,
678   south Eastern Desert, Egypt. In: Thorweile U, Schandeimeier H (eds)
679   Geoscientific research in northeast Africa, 31–34

680 Ueno H, Hisada KI, Ogawa Y (2011) Numerical estimation of duplex thickening in a
681   deep-level accretionary prism: A proposal for network duplex. GSA Special
682   Papers 480, 207-213.

683 Vail JR (1983) Pan-African crustal accretion in north-east Africa. J Afr Earth Sci 1: 285-
684   294.

685 Valli F, Guillot S, Hattori KH (2004) Source and tectono-metamorphic evolution of
686   mafic and politic metasedimentary belt, Archean Superior Province of Canada.
687   Precambrian Res 132: 155-177.

688 Workman, R.K. and Hart, S.R. (2005). Major and trace element composition of the
689   depleted MORB mantle (DMM). Earth Planet Sci Lett 231: 53-72.

690 Zoheir BA, Klemm DD (2007) The tectono-metamorphic evolution of the central part of
691   the Neoproterozoic Allaqi-Heiani suture, south Eastern Desert of Egypt. Gond
692   Res 12:289–304.

693

694   **List of Figs.**

695   **Fig. 1.** Distribution of the ophiolites in the Arabian-Nubian Shield (modified after Vail

696   1983; Abu-Alam et al. unpublished data).

697   **Fig. 2.** Geological map of Sol Hamed area modified after Abu El-Laban 2002.

698   **Fig. 3.** (a) Semi-schematic drawing showing the ophiolitic ultramafic of Sol Hamed area,

699   lizardite and anthophyllite are metamorphosed after orthopyroxene. Chrysotile is

700   metamorphosed after lizardite. Talc is after anthophyllite. Liz, opx, anth, mag

701   and s are lizardite, orthopyroxene, anthophyllite, magnesite and sulphites,

702   respectively. (b) Zoned spinel in Sol Hamed serpentinite. Darker zones are

703   richer in Cr.

704   **Fig. 4.** Mineral chemisty. a) Substitution in serpentine. Aluminum and chromium are

705   grouped together, as they tend to vary sympathetically. b) Compositional

706   changes in spinels expressed in a triangular $Cr-Fe^{3+}-Al^{3+}$ plot with reference to

707   the fields of spinel types: a-aluminian chromite, b-ferrian chromite, c-chromian

708   magnetit, d-aluminian magnetite, e-ferrian spinel and f-chromian spinel (Stevens

709   1944) and the different metamorphic facies defined by Purvis et al. (1972);

710   Evans and Frost (1975) and Suita and Streider (1996).

711   **Fig. 5.** Whole rock $MgO/SiO_2–Al_2O_3/SiO_2$ plot. The terrestrial array is a compilation of

712   subcontinental peridotites (Hart and Zindler 1986) and represents a melt

713   depletion trend. The Sol Hamed serpentinites plot offset to lower MgO/SiO_2

714   values because of alteration. Compositions of depleted MORB mantle (DMM;

31

715   Workman and Hart 2005), primitive mantle (PM; McDonough and Sun 1995)

716   and seafloor weathering trend (Snow and Dick 1995) are plotted for comparison.

717   **Fig. 6.** Composition of spinels compared with those in modern peridotites. Data are

718   plotted on 100Cr/Cr+Al (Cr#) vs. 100Mg/Mg+Fe (Mg#) diagram, modified after

719   Dick and Bullen (1984). The fields are after Bloomer et al. (1995).

720   **Fig. 7.** *P-T* grid in the system CFMASH for atg, chr, en, fs, di, hed, fo, fa, anth, tr, clin,

721   ta, sp, herc, mgts, fta, br, H_2O. Activity of the H_2O is imposed to be the unity.

722   Note: reactions liz = br atg, liz = chr, liz = ta fo clin H_2O are used here after

723   Evan 2004; Chernosky 1975; Caruso and Chernosky 1979, respectively.

724   **Fig. 8.** A simplified *P-T* grid of Figure 7 shows only the interesting metamorphic

725   reactions. Maximum pressure during the cooling path is the pressure equivalent

726   to the invariant point [atg chr fs di hed fa tr ta herc fta br mgts]. The vertical bar

727   below the op. cit. invariant point shows the pressure equivalents to the Arabian-

728   Nubian Shield's ophiolitic crustal thicknesses as reconstructed by Stern et al.

729   (2004). The two gray arrows show the modern thermal gradient and ancient

730   thermal gradient. The black arrow showing the path of the study samples, the

731   peak pressure is 5-5.7 kbar based on the pressure calculation from Wadi

732   Haimur-Abu Swayel ophiolites (El-Naby and Frisch 1999). Note: the ancient

733   thermal gradient is equivalent to thickening of the sequence by factor of 5.5 as

734   suggest by Ueno et al. (2011). The temperature axe is in two different scales to

735   show the reactions at high temperature condition in more details than Figure 7.

736   **Fig. 9.** A *T-X*CO_2 grid in the system CFMASH-CO_2 for the following end-members:

737   anth, atg, chr, en, fs, di, hed, fo, fa, ta, sp, herc, mgts, fta, mag, sid, H_2O, CO_2.

738   The grid was constructed at 1 kbar. Fluid concentration is buffered by the

739   metamorphic reactions. The grid shows high CO_2 concentration in the fluid

740   **Fig. 10.** A three dimensional model illustrating the tectonic evolution of the studied

741   ophiolites. a) Development of subduction zone. High concentrated CO_2 fluid is

742   released from carbonate rocks in the subduction zone. These fluids re-

743   concentrated in the fore-arc ophiolites. A passive margin is drawn on the flank

744   of the oceanic basin since some authors recorded volcanic and sedimentary

745   rocks in the Arabian-Nubian Shield were formed in a passive margin setting

746   (e.g. Nakasib suture; Abdelsalam and Stern 1993). b) Thrusting and duplex

747   thickening of the ophiolitic sequence. The white star is the position of the

748   studied ophiolites.

749

Primary minerals	Olivine
	Opx
	Spinel
	Chromite (the inner core)
First stage of alteration and metamorphism	Lizardite
	Antigorite
	Anthophyllite
	Magnesite
	Magnetite
	Chromite (inter. zone)
	Sulphides
Second stage of alteration and metamorphism	Lizardite
	Chrysotile
	Talc
	Magnesite
	Magnetite
	Chromite (outer zone)

Table 1
Abu-Alam and Hamdy (2013)

Fluid interaction in the Arabian-Nubian Shield ophiolites

	Opx		Serpentine													
Sample	325/1	325/2	323	324	324	324	325	325	333	333	278	278	310	347	347	369	369
SiO_2	58.21	58.37	43.73	41.86	42.62	41.13	42.47	42.6	40.62	43.78	44.54	43.04	43.96	41.56	41.3	43.23	41.94
TiO_2	0.12	0.09	0.12	b.d.l	0.01	0.03	b.d.l	0.01	0.12	0.08	0.07	0.15	0.08	0.01	b.d.l	b.d.l	0.03
Al_2O_3	0.74	0.67	0.48	0.46	1.12	1.79	0.13	b.d.l	0.3	0.06	0.28	0.14	0.14	0.14	0.26	0.21	0.28
Cr_2O_3	0.42	0.36	b.d.l	b.d.l	0.16	0.02	0.02	b.d.l	0.22	b.d.l	b.d.l	0.34	0.12	0.09	0.16	0.15	0.36
FeO	4.85	5.09	2.61	2.88	1.98	3.33	1.81	2.05	4.2	2.66	1.37	1.85	0.94	3.99	3.36	2.11	6.21
MnO	0.03	0.07	0.09	b.d.l	0.04	b.d.l	b.d.l	b.d.l	0.38	b.d.l	0.01	0.09	b.d.l	0.17	0.22	0.01	b.d.l
MgO	34.99	35.1	37.04	37.04	37.67	36.99	38.42	36.68	34.37	37.74	37.78	36.88	38.14	38.06	38.68	37.17	35.98
CaO	b.d.l	0.03	b.d.l	0.1	b.d.l	b.d.l	b.d.l	0.19	0.03	0.07	0.06	0.13	b.d.l	b.d.l	b.d.l	0.18	0.11
Na_2O	b.d.l	b.d.l	0.13	0.01	0.05	0.05	0.02	b.d.l	b.d.l	0.12	0.01	0.01	0.1	b.d.l	b.d.l	0.09	0.08
K_2O	b.d.l	b.d.l	b.d.l	0.02	0.03	b.d.l	0.01	0.03	b.d.l	0.01	0.02	0.03	0.08	0.01	b.d.l	0.08	0.01
Total	99.36	99.78	84.2	82.37	83.68	83.34	82.88	81.56	80.24	84.52	84.14	82.66	83.56	84.03	83.98	83.23	85
Si	2	2	8.381	8.237	8.211	8.027	8.258	8.41	8.283	8.369	8.47	8.385	8.418	8.097	8.036	8.375	8.162
Ti	0.003	0.002	0.017	-	0.001	0.004	-	0.001	0.018	0.012	0.01	0.022	0.012	0.001	-	-	0.004
Al	0.03	0.027	0.108	0.107	0.254	0.411	0.03	-	0.072	0.014	0.063	0.032	0.032	0.032	0.06	0.048	0.064
Cr	0.011	0.01	-	-	0.024	0.003	0.003	-	0.035	-	-	0.052	0.018	0.014	0.025	0.023	0.055
Fe	0.139	0.146	0.418	0.474	0.319	0.543	0.294	0.338	0.716	0.425	0.218	0.301	0.151	0.65	0.547	0.342	1.011
Mn	0.001	0.002	0.015	-	0.007	-	-	-	0.066	-	0.002	0.015	-	0.028	0.036	0.002	-
Mg	1.792	1.792	10.58	10.86	10.82	10.76	11.13	10.79	10.44	10.75	10.71	10.71	10.88	11.05	11.21	10.73	10.43
Ca	-	0.001	-	0.021	-	-	-	0.04	0.007	0.014	0.012	0.027	-	-	-	0.037	0.023
Na	-	-	0.048	0.004	0.019	0.019	0.008	-	-	0.044	0.004	0.004	0.037	-	-	0.034	0.03
K	-	-	-	0.005	0.007	-	0.002	0.008	-	0.002	0.005	0.007	0.02	0.002	-	0.02	0.002
Cations	3.977	3.98	19.57	19.71	19.66	19.77	19.73	19.59	19.65	19.64	19.49	19.56	19.58	19.88	19.92	19.62	19.79
en	0.93	0.92															
fs	0.0055	0.006															
mgts	0.027	0.01															

Table 2
Abu-Alam and Hamdy (2013)

Fluid interaction in the Arabian-Nubian Shield ophiolites

	Talc								
Sample	306/2	306/2	306/2	306/2	306/2	347/2	347/2	347/2	347/2
SiO_2	61.07	60.04	60.92	59.98	61.09	56.78	57.36	57.22	57.21
TiO_2	0.05	b.d.l	0.04	0.07	0.22	b.d.l	b.d.l	b.d.l	b.d.l
Al_2O_3	0.03	0.14	0.28	0.05	b.d.l	0.42	0.5	0.37	0.34
Cr_2O_3	0.02	0.14	0.26	0.03	b.d.l	0.28	0.2	0.21	0.17
Fe_2O_3	b.d.l	b.d.l	b.d.l	b.d.l	b.d.l	0.68	0.64	0.64	0.62
FeO	3.31	3.61	3.85	2.71	3.11	5.54	5.22	5.16	5.04
MnO	b.d.l	b.d.l	0.04	b.d.l	b.d.l	b.d.l	0.16	b.d.l	0.2
MgO	27.14	26.91	26.85	27.17	27.6	34.4	34.26	34.41	34.84
CaO	0.09	0.02	b.d.l	0.15	0.16	b.d.l	b.d.l	b.d.l	b.d.l
Na_2O	0.13	b.d.l	0.16	0.17	0.13	b.d.l	b.d.l	b.d.l	b.d.l
Totals	91.84	90.86	92.4	90.33	92.31	98.1	98.34	98	98.42
Si	4.053	4.036	4.034	4.041	4.035	3.646	3.666	3.667	3.654
Ti	0.002	-	0.002	0.004	0.011	-	-	-	-
Al	0.002	0.011	0.022	0.004	-	0.032	0.038	0.028	0.026
Cr	0.001	0.007	0.014	0.002	-	0.014	0.01	0.011	0.009
Fe^{3+}	-	-	-	-	-	0.033	0.031	0.031	0.03
Fe^{2+}	0.184	0.203	0.213	0.153	0.172	0.297	0.279	0.276	0.269
Mn	-	-	0.002	-	-	-	0.009	-	0.011
Mg	2.685	2.696	2.65	2.728	2.717	3.292	3.263	3.286	3.316
Ca	0.006	0.001	-	0.011	0.011	-	-	-	-
Na	0.017	-	0.021	0.022	0.017	-	-	-	-
Sum	6.951	6.955	6.957	6.964	6.962	7.316	7.296	7.3	7.315
ta	0.71	0.72	0.68	0.75	0.74	0.83	0.83	0.85	0.85
fta	0.00023	0.00031	0.00036	0.00013	0.00019	0.00061	0.00052	0.00051	0.00046

Table 3
Abu-Alam and Hamdy (2013)

Fluid interaction in the Arabian-Nubian Shield ophiolites

Table

	Carbonate minerals												
Sample	300	300	300	306	306	306	306	306	306	368	368	368	368
SiO$_2$	0.19	0.15	0.04	0.11	0.23	0.18	0.05	0.04	0.09	0.13	0.16	0.1	0.09
Cr$_2$O$_3$	0.11	0.04	0.09	b.d.l	0.07	b.d.l	b.d.l	b.d.l	b.d.l	0.05	0.04	0.02	0.07
FeO	13.47	11.17	13.42	14.1	12.33	8.46	13.03	13.08	13.79	8.97	13.06	13.95	10.63
MnO	0.09	0.25	0.13	0.33	0.33	0.22	0.03	0.08	0.17	0.24	0.25	0.25	0.27
MgO	36.19	38.06	36.82	35.53	36.53	40.14	36.57	36.09	36.63	39.53	36.58	36.08	38.07
CaO	0.11	0.23	0.17	0.15	0.15	0.24	0.04	0.21	0.27	0.17	0.21	0.21	0.15
Totals	50.16	49.9	50.67	50.22	49.64	49.24	49.72	49.5	50.95	49.09	50.3	50.61	49.28
Si	0.006	0.004	0.001	0.003	0.007	0.005	0.002	0.001	0.003	0.004	0.005	0.003	0.003
Cr	0.003	0.001	0.002	-	0.002	-	-	-	-	0.001	0.001	0	0.002
Fe^{2+}	0.343	0.28	0.338	0.361	0.315	0.21	0.333	0.336	0.346	0.224	0.331	0.354	0.269
Mn	0.002	0.006	0.003	0.009	0.009	0.006	0.001	0.002	0.004	0.006	0.006	0.006	0.007
Mg	1.643	1.701	1.65	1.622	1.663	1.772	1.664	1.653	1.638	1.759	1.65	1.63	1.715
Ca	0.004	0.007	0.005	0.005	0.005	0.008	0.001	0.007	0.009	0.005	0.007	0.007	0.005
Sum	2	2	2	2	2	2	2	2	2	2	2	2	2
mag	0.84	0.86	0.84	0.83	0.84	0.89	0.85	0.84	0.83	0.89	0.84	0.83	0.87
sid	0.26	0.21	0.25	0.27	0.24	0.17	0.25	0.25	0.26	0.18	0.25	0.26	0.21

Table 4
Abu-Alam and Hamdy (2013)

Fluid interaction in the Arabian-Nubian Shield ophiolites

							Spinel										
	core02	rim03	core05	rim06	rim	core	core-rim	rim	core	core-rim	rim	core	core-rim	rim	core	core-rim	rim
SiO_2	0,07	0,05	0,07	0,23	0,13	0,24	b.d.l	0,21	0,05	0,02	0,22	0,19	0,12	0,21	0,22	0,04	0,35
TiO_2	0,36	0,23	0,21	0,18	b.d.l	0,22	0,27	b.d.l	0,15	b.d.l	0,02	0,21	0,13	b.d.l	0,08	0,11	b.d.l
Al_2O_3	8,81	9,23	8,28	8,4	b.d.l	6,27	6,32	0,12	5,4	6,53	0,1	6,67	6,5	b.d.l	5,57	6,49	0,15
FeO	34,12	34,47	31,23	32,51	89,78	32,88	31,47	90,89	34,12	32,71	91,34	31,6	32,14	90,03	30,39	30,7	90,16
Cr_2O_3	51,38	51,1	53,76	52,76	1,64	56,51	56,62	1,56	56,25	55,26	1,34	55,82	55	2,1	56,98	56,84	0,75
MnO	0,39	b.d.l	0,36	0,51	0,46	0,18	0,92	0,5	0,02	0,54	0,41	0,66	1,09	0,45	0,85	0,25	0,11
MgO	4,23	4,03	4,96	4,56	1	4,03	4,52	0,88	3,67	4,4	1,05	4,07	4,06	0,75	4,53	5,17	1,03
NiO	b.d.l	0,72	0,48	0,17	0,35	b.d.l	0,22	0,72	0,01	b.d.l	0,23	0,02	0,25	0,38	0,34	b.d.l	0,46
Total	99,36	99,83	99,35	99,32	93,36	100,33	100,34	94,88	99,67	99,46	94,71	99,24	99,29	93,92	98,96	99,6	93,01
Si	0,02	0,014	0,02	0,065	0,052	0,068	-	0,083	0,014	0,006	0,087	0,054	0,035	0,084	0,063	0,011	0,141
Al	2,96	3,084	2,76	2,809	-	2,099	2,113	0,056	1,84	2,207	0,047	2,249	2,203	-	1,889	2,17	0,071
Ti	0,08	0,049	0,045	0,038	-	0,047	0,058	-	0,033	-	0,006	0,045	0,028	-	0,017	0,023	-
Cr	11,56	11,451	12,018	11,83	0,522	12,687	12,692	0,488	12,852	12,526	0,42	12,623	12,499	0,663	12,956	12,744	0,239
Mn	0,094	-	0,086	0,123	0,157	0,043	0,221	0,168	0,005	0,131	0,138	0,16	0,266	0,152	0,207	0,06	0,038
Mg	1,796	1,705	2,093	1,93	0,6	1,708	1,913	0,52	1,583	1,883	0,621	1,737	1,742	0,447	1,944	2,188	0,62
Ni	-	0,16	0,11	0,04	0,11	-	0,05	0,23	-	-	0,07	-	0,06	0,12	0,08	-	0,15
Fe^{2+}	6,11	6,135	5,711	5,907	7,133	6,249	5,816	7,082	6,412	5,986	7,171	6,103	5,932	7,281	5,769	5,752	7,192
Fe^{3+}	1,39	1,402	1,157	1,258	15,426	1,099	1,137	15,373	1,261	1,261	15,44	1,029	1,235	15,253	1,075	1,052	15,549
Mg#	0,227	0,217	0,268	0,246	0,079	0,214	0,247	0,068	0,197	0,239	0,079	0,221	0,227	0,057	0,252	0,275	0,079
Cr#	0,726	0,718	0,754	0,744	0,0321	0,798	0,796	0,030	0,805	0,783	0,026	0,793	0,784	0,041	0,813	0,798	0,015
Fe^{3+}#	0,087	0,087	0,072	0,079	0,967	0,069	0,071	0,965	0,079	0,078	0,970	0,064	0,077	0,958	0,067	0,065	0,980
mt	0.004	0.006	0.005	0.004	0.90	0.0013	0.0015	0.90	-	0.0009	0.89	0.0026	0.0012	0.90	0.0008	0.0018	0.91
cmt	0.39	0.39	0.41	0.40	0.00058	0.48	0.46	0.00052	0.50	0.45	0.0004	0.47	0.46	0.001	0.48	0.45	0.0001

Table 5
Abu-Alam and Hamdy (2013)

Fluid interaction in the Arabian-Nubian Shield ophiolites

Oxide	306	347	369	310
TiO_2	0.06	0.02	0.01	0.04
SiO_2	41.49	38.41	38.55	38.00
Al_2O_3	0.48	0.31	0.80	0.88
Fe_2O_3	6.79	7.54	8.70	7.49
MnO	0.09	0.09	0.09	0.07
MgO	38.99	38.43	39.83	39.11
CaO	0.18	1.19	0.65	0.12
Na_2O	0.09	b.d.l	0.01	0.17
K_2O	0.01	b.d.l	0.01	0.05
Sum	88.19	86.00	88.65	85.94
LOI	10.60	12.99	10.27	13.14
Cr	2742.20	2717.47	2703.71	2696.98
Co	166.79	154.23	116.20	120.41
Ni	2381.21	2060.51	1650.08	1799.16
Cu	63.83	8.27	46.32	14.97
Zn	57.11	16.55	11.98	13.32
Sr	55.04	89.11	48.08	46.61
V	40.31	14.00	33.93	29.83
Ba	35.24	45.00	20.00	15.00
Pb	4.70	4.63	24.04	13.15
Cd	2.00	3.31	3.43	2.00
Li	10.08	9.93	1.68	4.99
Rb	1.80	0.86	0.17	0.97

Table 6
Abu-Alam and Hamdy (2013)
Fluid interaction in the Arabian-Nubian Shield ophiolites

Figure

Fig. 1
Abu-Alam and Hamdy (2013)

Fluid interaction in the Arabian-Nubian Shield ophiolites

Figure

Fig. 2
Abu-Alam and Hamdy (2013)

Fluid interaction in the Arabian-Nubian Shield ophiolites

Figure

(a)

~ 5 mm

(b)

⌒ Chrysotile	⬡ Chlorite
Olivine	Talc
Zoned Chromite	Magnetite and spinel

Figure

(a) Fe+Mn   Mg   Al+Cr

(b) Cr³⁺   Fe³⁺   Al³⁺

Core   intermediate zone   rim
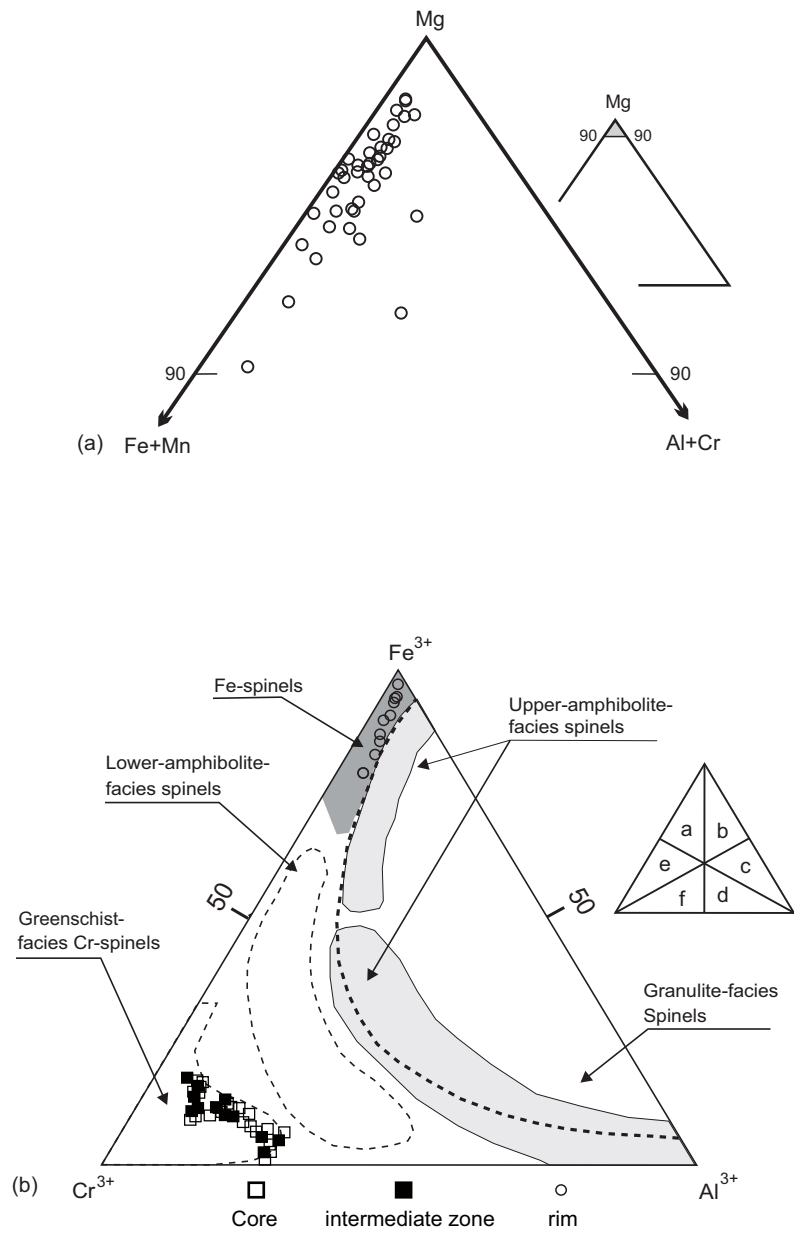
Fig. 4
Abu-Alam and Hamdy (2013)

Fluid interaction in the Arabian-Nubian Shield ophiolites

Figure
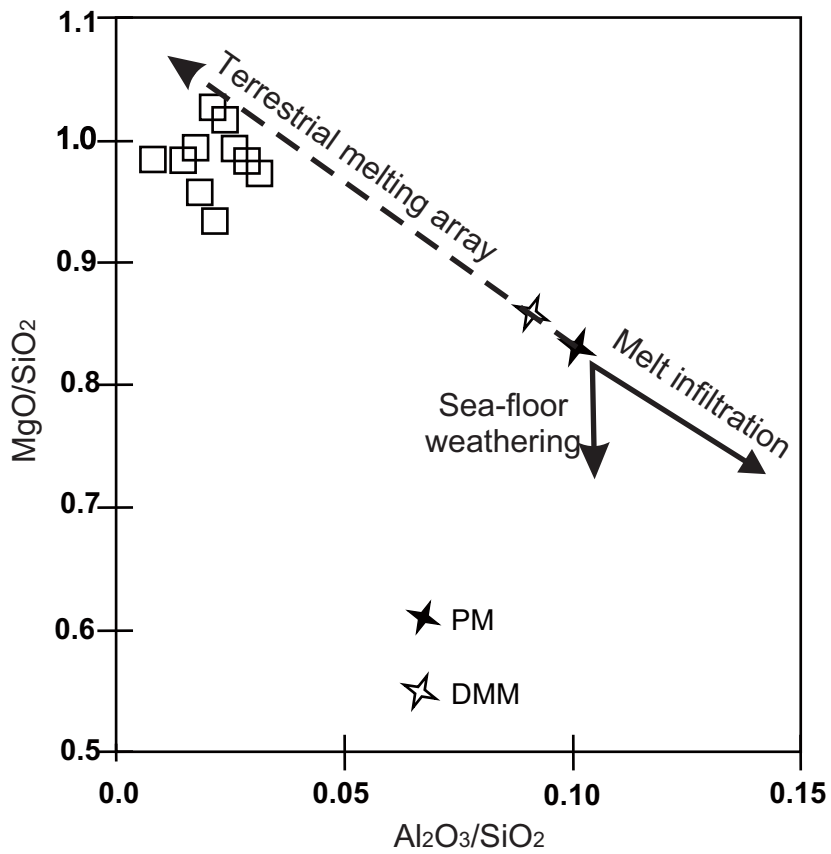
Fig. 5
Abu-Alam and Hamdy (2013)

Fluid interaction in the Arabian-Nubian Shield ophiolites
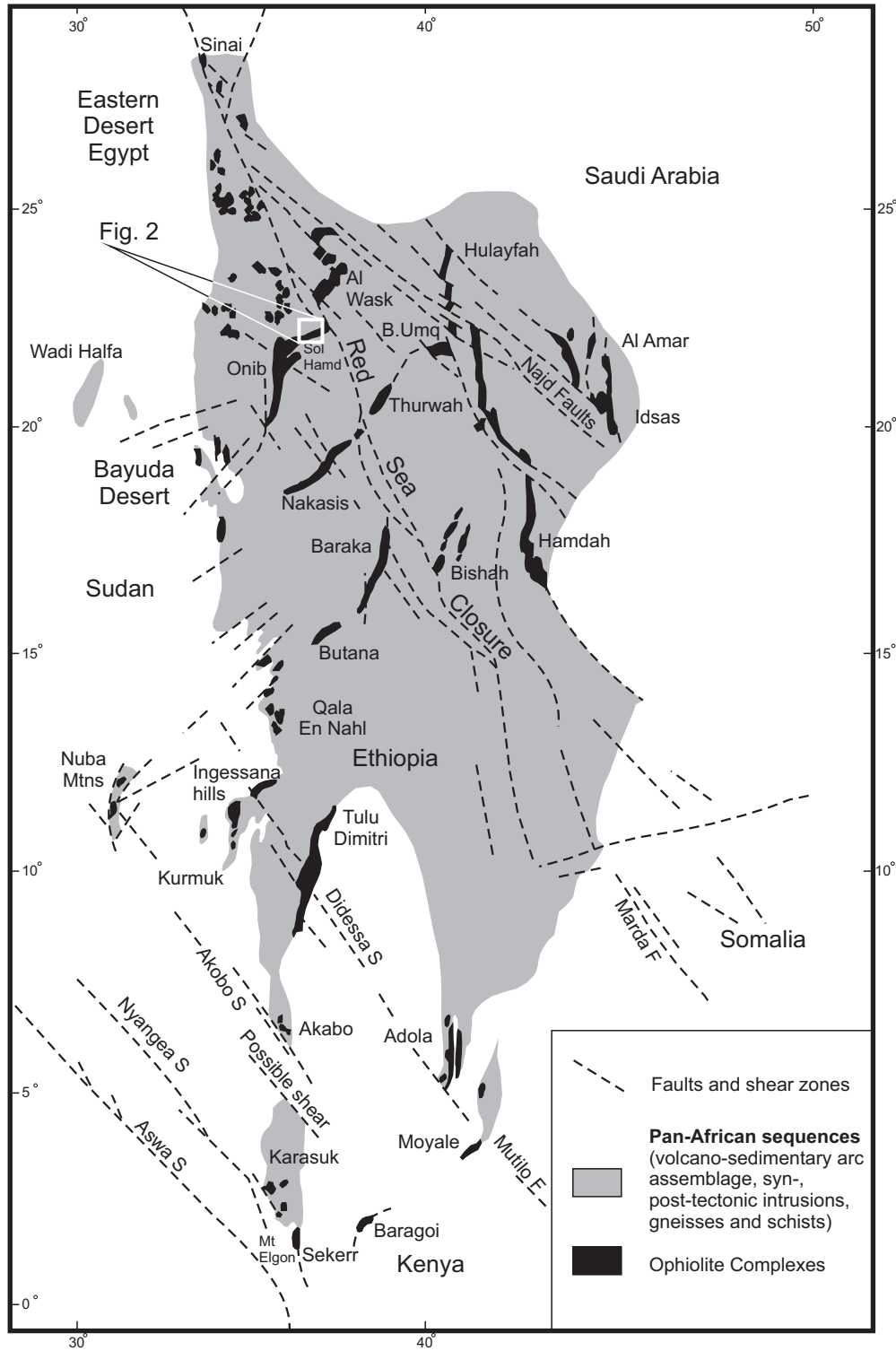
Figure

Fig. 6
Abu-Alam and Hamdy (2013)

Fluid interaction in the Arabian-Nubian Shield ophiolites

Figure

CFMASH

P (bar)

6200
5700
5200
4700
4200
3700
3200
2700
2200
1700
1200
700
200

1) tr fo = di en H$_2$O
2) fa anth = fs en H$_2$O
3) clin = sp fo en H$_2$O
4) fo anth = en H$_2$O
5) clin = sp fo anth H$_2$O
6) tr fa = di en fs H$_2$O
7) clin fa = herc fo anth H$_2$O
8) sp fo ta = clin anth
9) fa ta = fs anth H$_2$O
10) clin fa ta = anth herc H$_2$O
11) tr hed fa = di fs H$_2$O
12) clin anth = sp en H$_2$O
13) clin fa = herc fo en H$_2$O
14) di clin fa = herc tr fo H$_2$O
15) clin ta = H$_2$O sp anth

16) clin anth fa = herc en H$_2$O
17) di clin = sp tr fo H$_2$O
18) fta atg = H$_2$O ta fa
19) hed br atg = H$_2$O di fa
20) fa fta = H$_2$O fs
21) di mgts clin = H$_2$O tr sp
22) hed br clin = H$_2$O di herc fa
23) fta clin = H$_2$O herc ta fs
24) mgts clin = H$_2$O ta sp
25) br atg = H$_2$O fo
26) herc ta hed = H$_2$O mgts tr fs
27) br fa clin = herc fo H$_2$O
28) clin br = H$_2$O sp fo
29) herc fta ta = H$_2$O mgts fs
30) ta sp = H$_2$O mgts anth

Reaction equations are written with the high T assemblage to the right of the equal sign

[atg chr fs di hed fa tr clin sp herc fta br mgts]

clin hed H$_2$O herc di tr fa

atg fo ta H$_2$O

fs clin

herc fa ta H$_2$O

en ta anth

liz = br atg (Evan, 2004)

liz = chr (Chernosky, 1975)

liz = ta fo clin H$_2$O (Caruso & Chernosky, 1979)

chr H$_2$O fo atg

hed atg ta

H$_2$O tr fa

hed atg

H$_2$O di tr fa

hed fa ta tr fs H$_2$O

clin en sp fo ta

clin hed ta H$_2$O herc tr fs

clin en fa herc fo ta

di atg tr fo H$_2$O

clin en fa herc fo anth

fo ta anth H$_2$O

clin en sp fo anth

clin hed fs herc tr fa H$_2$O

clin anth fa herc fo ta

[atg chr fs di hed tr ta sp fta br mgts]

[atg chr fs di hed tr sp H$_2$O fta br mgts]

[atg chr fs di hed fa tr ta herc fta br mgts]

[atg chr fs di herc hed tr fa H$_2$O fta br mgts]

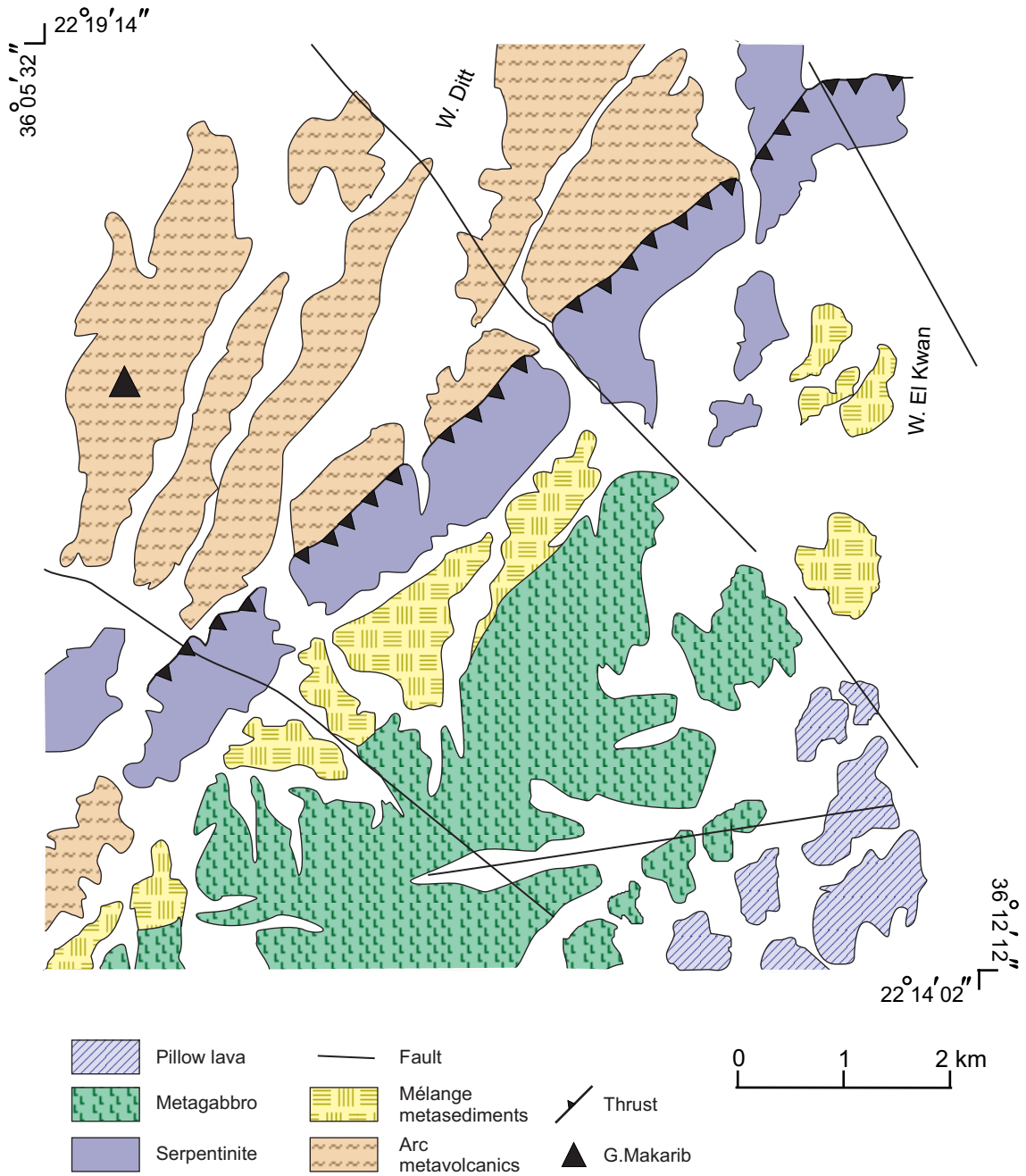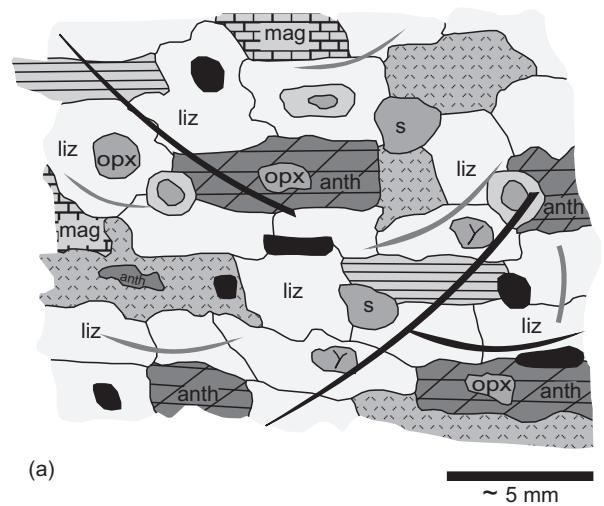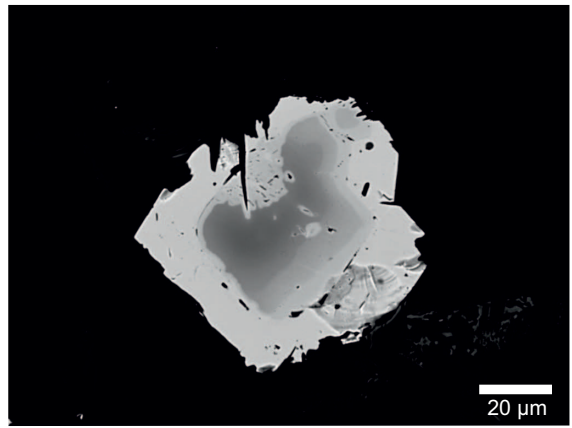100 150 200 250 300 350 400 450 500 550 600 650 700 750 T °C

Fig. 7
Abu-Alam and Hamdy (2013)

Fluid interaction in the Arabian-Nubian Shield ophiolites

Figure

CFMASH

P (bar)

2) fa anth = fs en H_2O
4) fo anth = en H_2O
8) sp fo ta = clin anth
9) fa ta = fs anth H_2O
10) clin fa ta = anth herc H_2O

12) clin anth = sp en H_2O
15) clin ta = H_2O sp anth
16) clin anth fa = herc en H_2O
30) ta sp = H_2O mgts anth

Reaction equations are written with the high T assemblage to the right of the equal sign

6200
5700
5200
4700
4200
3700
3200
2700
2200
1700
1200
700
200

Modern thermal gradient 10 °C/km
Thermal gradient 25 °C/km
Ancient thermal gradient 30 °C/km

5.5 thickened prism
3.5 thickened prism

liz = br atg (Evan, 2004)
liz = ta fo clin H_2O (Caruso & Chernosky, 1979)
liz = chr (Chernosky, 1975)

clin en fa herc fo ta
clin en sp fo ta
en ta anth
clin anth fa herc fo ta

en ta anth
fo ta anth H_2O

clin en fa herc fo anth
clin en sp fo anth

[atg chr fs di hed fa tr clin sp herc fta br mgts]
[atg chr fs di hed tr ta sp fta br mgts]
[atg chr fs di hed fa tr ta herc fta br mgts]
[atg chr fs di hed tr sp H_2O fta br mgts]
[atg chr fs di herc hed tr fa H_2O fta br mgts]

4
9
10
16
12
15
30
8
4
2

100 200 300 400 500 600 650 700 750 T°C

Fig. 8
Abu-Alam and Hamdy (2013)

Fluid interaction in the Arabian-Nubian Shield ophiolites

Figure

CFMASH-CO$_2$

T °C

at 1 kbar

750

700

⑭

650

600

550

[atg chr fs
di hed fa
sp herc mgts
fta mag
sid CO$_2$]

⑬

⑫

⑰

⑯

⑮

[atg chr di
hed fo fa
sp fta mag
sid CO$_2$]

[atg chr hed fo
sp mgts fta
mag sid CO$_2$]

⑪

[atg chr fs di hed
fo fa herc fta
mag sid CO$_2$]

⑳

⑩

500

⑲

⑦

⑱

⑧

②

㉑

㉒

⑨

450

[atg chr fs
di hed fa
sp herc
mgts fta sid]

⑤

④

fa CO$_2$
fs sid

[atg chr fs di
hed fo sp herc
mgts fta]

⑥

③

[atg chr di
hed fo sp
herc mgts
fta mag]

①

400

fs di CO$_2$ H$_2$O
hed ta sid

350

300

fs CO$_2$ H$_2$O
fta sid

250

1) ta sid = en fs CO$_2$ H$_2$O

9) fo ta = en H$_2$O

16) ta herc = mgts anth fs H$_2$O

2) fa ta = en fs H$_2$O

10) ta herc fta = fs mgts H$_2$O

17) herc anth = mgts en fs H$_2$O

200

3) ta sid = en fa CO$_2$ H$_2$O

11) hed ta herc = fs di mgts H$_2$O

18) ta en = anth H$_2$O

4) ta mag = en CO$_2$ H$_2$O

12) ta fa = fs anth H$_2$O

19) ta fo = anth H$_2$O

5) ta sid = fa mag CO$_2$ H$_2$O

13) anth fa = en fs H$_2$O

20) fo anth = en H$_2$O

150

6) en sid = fa mag CO$_2$

14) ta sp = mgts anth H$_2$O

21) sp ta = en mgts H$_2$O

7) ta mag = fo CO$_2$ H$_2$O

15) sp anth = mgts en H$_2$O

22) herc ta = en mgts fs H$_2$O

8) en mag = fo CO$_2$

Reaction equations are written with the high T assemblage to the right of
the equal sign

100

0.88   0.90   0.92   0.94   0.96   0.98   XCO$_2$

Fig. 9
Abu-Alam and Hamdy (2013)

Fluid interaction in the Arabian-Nubian Shield ophiolites

Figure

East-Gondwana

Mozambique Ocean

passive margin

Volcanic arc

Accretionary prism

Forearc basin

Oceanic crust

CO₂ rich fluid

(a)

East-Gondwana

Ophiolites with mid-oceanic ridge setting
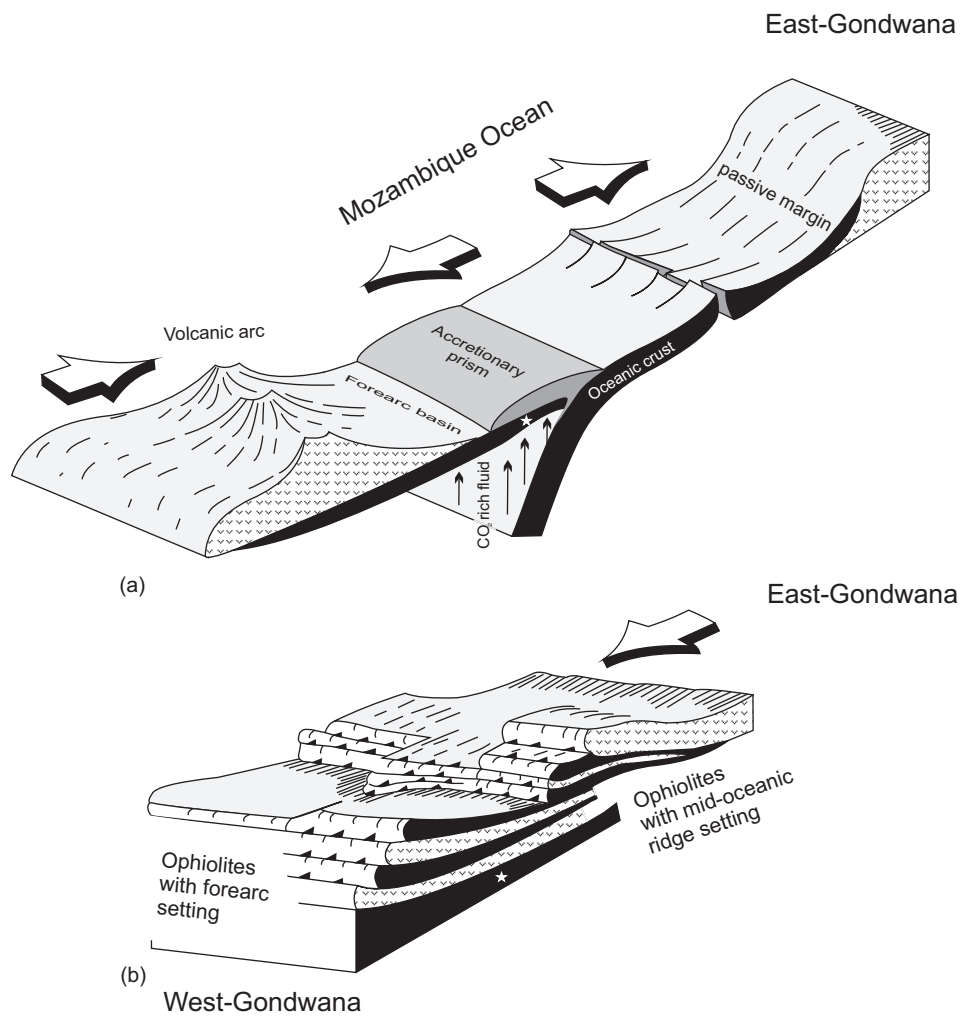
Ophiolites with forearc setting

(b)

West-Gondwana

Fig. 10
Abu-Alam and Hamdy (2013)

Fluid interaction in the Arabian-Nubian Shield ophiolites